AERODYNAMIC HEATING ON BLUNT NOSE SHAPES IN RAREFIED HYPERSONIC FLOW

Wilson F. N. Santos
National Institute for Space Research
Combustion and Propulsion Laboratory
12630-000 Cachoeira Paulista, SP, Brazil
wilson@lcp.inpe.br

Abstract. The steady-state aerodynamic characteristics of a new family of blunted leading edges immersed in high-speed rarefied air flow are examined by using a Direct Simulation Monte Carlo Method. A very detailed description of the flow properties has been presented separately in the vicinity of the leading edge by a numerical method that properly accounts for nonequilibrium effects that arise near the leading edge and that are especially important at high Mach number. Comparisons based on geometry are made between these new blunt configuartions and circular cilynder shapes. Some significant differences between these shapes is noted on the flowfield structure and on the aerodynamic surface quantities. It is found that the upstream effects have different influence on velocity, density, pressure and temperature along the stagnation streamline ahead of the leading edges. The analysis also shows that, despite the seeming advantages of the new blunt shapes, circular cylinder still provides smaller stagnation point heating, however large total drag under the range of condition investigated.

Keywords. *DSMC, aerodynamic heating, hypersonic flow, rarefied flow, blunt leading edge.*

1. Introduction

At hypersonic flight speeds, the vehicle leading edges must be blunt to some extent in order to reduce the heat transfer rate to acceptable levels and to allow for internal heat conduction. The use of blunt-nose shapes tends to alleviate the aerodynamic heating problem since the heat flux for blunt bodies is far lower than that for sharply pointed bodies. In addition, the reduction in heating rate for a blunt body is accompanied by an increase in heat capacity, due to the increased volume. Due mainly to manufacturing problems and the extremely high temperatures attained in hypersonic flight, hypersonic vehicles will have blunt nose, although probably slendering out at a short distance from the nose. Therefore, designing a hypersonic vehicle leading edge involves a tradeoff between making the leading edge sharp enough to obtain acceptable aerodynamic and propulsion efficiency and blunt enough to reduce the aerodynamic heating in the stagnation point.

A method of designing low heat transfer bodies is devised on the premise that the rate of heat transfer to the nose will be low if the local velocity is low, while the rate of heat transfer to the afterbody will be low if the local density is low (Reller, 1957). A typical body that results from this design method consists of a flat nose followed by a highly curved, but for the most part slightly inclined, afterbody surface. In order to avoid possible separation and reattachment due to the junction flat nose/afterbody surface, it is desirable to have a contour that generates a continuously favorable pressure gradient. Such a contour was determined by Eggers et al. (1956) by using the modified Newtonian theory.

The purpose of this work is to examine computationally the flowfield structure for a family of these contours that satisfy these geometric constraints and to compare them to circular cylinder geometries in order to provide information on how well these shapes stand up as possible candidates for blunting geometries of hypersonic leading edges. The focus of the present study is the low-density region in the upper atmosphere, where numerical gaskinetic procedures are available to simulate hypersonic flows. High-speed flows under low-density conditions deviate from a perfect gas behavior because of the excitation of rotation, vibration and dissociation. At high altitudes, and therefore low density, the molecular collision rate is low and the energy exchange occurs under nonequilibrium conditions. In such a circumstance, the degree of molecular nonequilibrium is such that the Navier-Stokes equations are inappropriate. Therefore, a Direct Simulation Monte Carlo (DSMC) method will be employed to calculate the rarefied hypersonic two-dimensional flow on the leading edge shapes.

2. Body Shape Definition

In dimensionless form, the contour that defines the shape of the afterbody surface is given by,

$$\bar{x} = \int_{\bar{y}=1}^{\bar{y}=\bar{y}_{\max}} \sqrt{\bar{y}^k - 1}\, d\bar{y} \tag{1}$$

where $\bar{x} = x/y_{nose}$ and $\bar{y} = y/y_{nose}$.

The blunt shapes are modeled by assuming a sharp leading edge of half angle θ with a circular cylinder of radius R inscribed tangent to the wedge. The blunt shapes, inscribed between the wedge and the cylinder, are also tangent to them at the same common point where they have the same slope angle. The circular cylinder diameter provides a reference for the amount of blunting desired on the leading edges. It was assumed a leading edge half angle of 10°, a circular cylinder diameter of 10^{-2}m and flat nose thicknesses t/λ_∞ of 0.01, 0.1 and 1.0, where $t = 2y_{nose}$ and λ_∞ is the

freestream mean free path. Figure 1(a) illustrates this construction for the set of shapes investigated. From geometric considerations, the exponent k in Eq. (1) is obtained by matching slope on the wedge, circular cylinder and on the body shapes at the tangency point. For dimensionless thicknesses of 0.01, 0.1 and 1.0, the exponent k corresponds to 0.501, 0.746 and 1.465, respectively. The common body height H and the body length L are obtained in a straightforward manner.

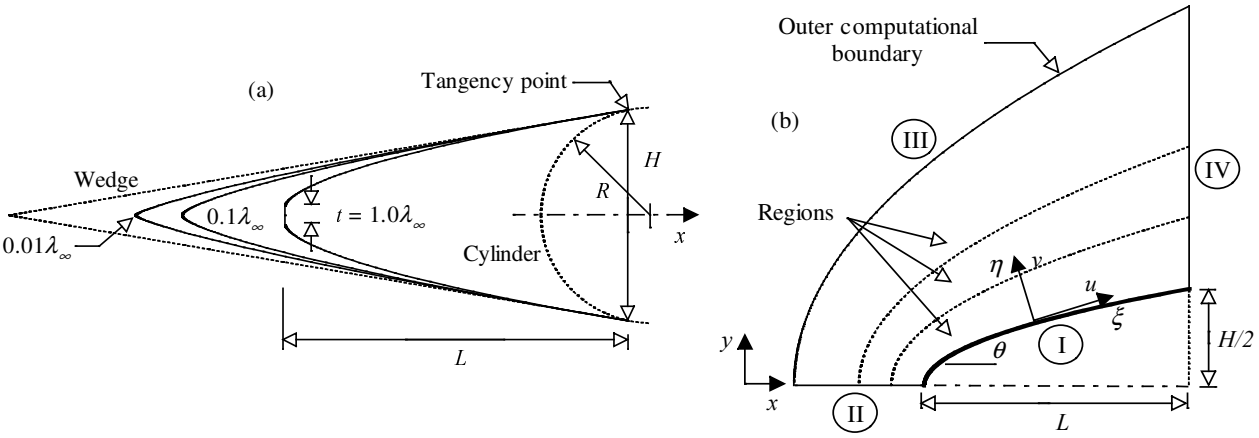

Figure 1: Drawing illustrating (a) the leading edge shapes and (b) the computational domain.

3. Computational Method and Procedure

The degree of departure of a flow from the continuum is indicated by the flow Knudsen number, $Kn = \lambda/l$, where λ is the mean free path and l is the characteristic length of the flow. Traditionally, flows are divided into four regimes (Schaff, 1958): $Kn < 0.01$, continuum flow, $0.01 < Kn < 0.1$, slip flow, $0.1 < Kn < 10$, transitional flow, and $Kn > 10$, free molecular flow.

The most successful numerical technique for modeling complex transitional flows has been the Direct Simulation Monte Carlo (DSMC) method (Bird, 1994). The DSMC method simulates real gas flows with various physical processes by means of a huge number of modeling particles, each of which is a typical representative of great number of real gas molecules. DSMC models the flow as being a collection of discrete particles, each one with a position, velocity and internal energy. The state of the particles is stored and modified with time as the particles move, collide, and undergo boundary interactions in simulated physical space.

The molecular collisions are modeled using the variable hard sphere (VHS) molecular model (Bird, 1981). This model employs the simple hard sphere angular scattering law so that all directions are equally possible for post-collision velocity in the center-of-mass frame of reference. However, the collision cross section depends on the relative speed of colliding molecules. The intermolecular collisions are uncoupled to the translational molecular motion over the time step used to advance the simulation. Time is advanced in discrete steps such that each step is small in comparison with the mean collision time (Bird, 1994). The simulation is always calculated as unsteady flow. However, a steady flow solution is obtained as the large time state of the simulation.

The energy exchange between kinetic and internal modes is controlled by the Borgnakke-Larsen statistical model (Borgnakke and Larsen, 1975). The essential feature of this model is that a part of collisions is treated as completely inelastic, and the remainder of the molecular collisions is regarded as elastic. Simulations are performed using a nonreacting gas model consisting of two chemical species, N_2 and O_2. Energy exchanges between the translational and internal modes are considered. The vibrational temperature is controlled by the distribution of energy between the translational and rotational modes after an inelastic collision. The probability of an inelastic collision determines the rate at which energy is transferred between the translational and internal modes after an inelastic collision. For a given collision, the probabilities are designated by the inverse of the relaxation numbers, which correspond to the number of collisions necessary, on average, for a molecule to relax. The relaxation numbers are traditionally given as constants, 5 for rotation and 50 for vibration.

The flowfield is divided into a number of regions, which are subdivided into computational cells. The cells are further subdivided into 4 subcells, 2 subcells/cell in each direction. The cell provides a convenient reference sampling of the macroscopic gas properties, while the collision partners are selected from the same subcell for the establishment of the collision rate. As a result, the flow resolution is much higher than the cell resolution. The dimensions of the cells must be such that the change in flow properties across each cell is small. The linear dimensions of the cells should be small in comparison with the scale length of the macroscopic flow gradients in the streamwise directions, which means that the cell dimensions should be of the order of the local mean free path or even smaller (Bird, 1994).

The computational domain used for the calculation is made large enough so that body disturbances do not reach the upstream and side boundaries, where freestream conditions are specified. A schematic view of the computational domain is depicted in Fig. 1(b). Side I is defined by the body surface. Diffuse reflection with complete thermal

accommodation is the condition applied to this side. Advantage of the flow symmetry is taken into account, and molecular simulation is applied to one-half of a full configuration. Thus, side II is a plane of symmetry. In such a boundary, all flow gradients normal to the plane are zero. At the molecular level, this plane is equivalent to a specular reflecting boundary. Side III is the freestream side through which simulated molecules enter and exit. Finally, the flow at the downstream outflow boundary, side IV, is predominantly supersonic and vacuum condition is specified (Bird, 1994). At this boundary, simulated molecules can only exit.

The freestream and flow conditions used in the present calculations are those given by Bertin (1994) and summarized in Tab. (1). The gas properties considered in the simulation are shown in Tab. (2). The freestream velocity V_∞, assumed to be constant at 3.56 km/s, corresponds to freestream Mach number M_∞ of 12. The wall temperature T_w is assumed constant at 880 K.

Table 1: Freestream Conditions

Temperature T_∞ (K)	Pressure p_∞ (N/m^2)	Density ρ_∞ (kg/m^3)	Number density n_∞ (m^{-3})	Viscosity μ_∞ (Ns/m^2)	Mean free path λ_∞ (m)	Velocity V_∞ (m/s)
220.0	5.582	8.753×10^{-5}	1.8209×10^{21}	1.455×10^{-5}	9.03×10^{-4}	3560

Table 2: Gas Properties

	Mole fraction X	Molecular mass m (kg)	Molecular diameter d (m)	Degree of freedom ζ
O_2	0.237	5.312×10^{-26}	4.01×10^{-10}	5
N_2	0.763	4.65×10^{-26}	4.11×10^{-10}	5

The overall Knudsen number Kn_t, defined as the ratio of the freestream mean free path λ_∞ to the leading edge thickness t, corresponds to 1, 10 and 100 for leading edge thicknesses t/λ_∞ of 1.0, 0.1 and 0.01, respectively. The Reynolds number Re_t covers the range from 0.193 to 19.3, based on conditions in the undisturbed stream with leading edge thickness t as the characteristic length.

4. Computational Results and Discussion

Attention is now focused on the calculations of the flowfield properties and aerodynamic surface quantities obtained from the DSMC results. The flowfield properties of particular interest in the transitional flow regime are the velocity, density, pressure and temperature. Aerodynamic surface quantities of particular interest are number flux, pressure, heat transfer, skin friction and drag. Therefore, the purpose of this section is to discuss differences in these properties due to variations in the leading edge thickness and to compare them to those obtained for the reference circular cylinder that generated the blunt shapes. Comparisons based on geometry are made to examine the benefits and disadvantages of using these blunt geometries over circular cylinders.

4.1. Flowfield Structure

Normal velocity profiles along the stagnation streamline and their dependence on the leading edge thickness are illustrated in Fig. (2a). Each profile has been taken through cell centroids that lie very close to the stagnation line, and therefore can be considered as being along the stagnation streamline. In Fig. (2a), the normal velocity v is expressed as a fraction of the freestream velocity V_∞, and $\eta\lambda_\infty$ is the dimensionless distance upstream the leading edges.

In simulating rarefied flows, the computational flow domain must extent far enough upstream of the body in order to provide ample opportunity for freestream molecules to interact with those molecules that have reflected from the body and are diffusing into the flow. Insufficient upstream domain size leads to overprediction of aerodynamic heating and forces (Haas and Fallavollita, 1994). Figure (2a) demonstrates that the leading edge thickness influences the flowfield far upstream. This domain of influence increases with increasing the leading edge thickness. This results from the upstream diffusion of particles that are reflected from the nose of the leading edge. Consequently, blunting the nose of the body (increasing t) leads to significantly larger disturbance upstream of the body. For instance, the upstream distance for a velocity reduction of 1% ($v/V_\infty = 0.99$) is around $2.7\lambda_\infty$, $3.2\lambda_\infty$ and $5.1\lambda_\infty$ for cases $t/\lambda_\infty = 0.01$, 0.1 and 1.0, respectively, and $8.7\lambda_\infty$ for the cylinder.

Figure (2b) displays the velocity slip u_w profiles, normalized by the freestream velocity V_∞, along the body surface as a function of the dimensionless arc length s/λ_∞ measured from the stagnation point. It is seen that velocity slip increases from zero at the stagnation point up to a maximum value on the afterbody surface far downstream from the nose of the leading edge. For the leading edge thicknesses investigated, the maximum value for the velocity slip takes place at a station that corresponds to a body slope of 20°. For the bluntest case, $t/\lambda_\infty = 1.0$, the flow expands slowly, and the maximum velocity slip is around 7% of the freestream velocity. For the sharpest case, $t/\lambda_\infty = 0.01$, the maximum velocity slip is around 12% of the freestream velocity. Hence, it means that the outer extent of the flowfield disturbance

above the surface is much smaller for the sharp leading edge case (t/λ_∞ = 0.01) than that for the blunt leading edge case (t/λ_∞ = 1.0). For the cylinder, the velocity slip increases monotonically along the cylindrically blunt portion up to the cylinder/wedge junction, where it takes the maximum value.

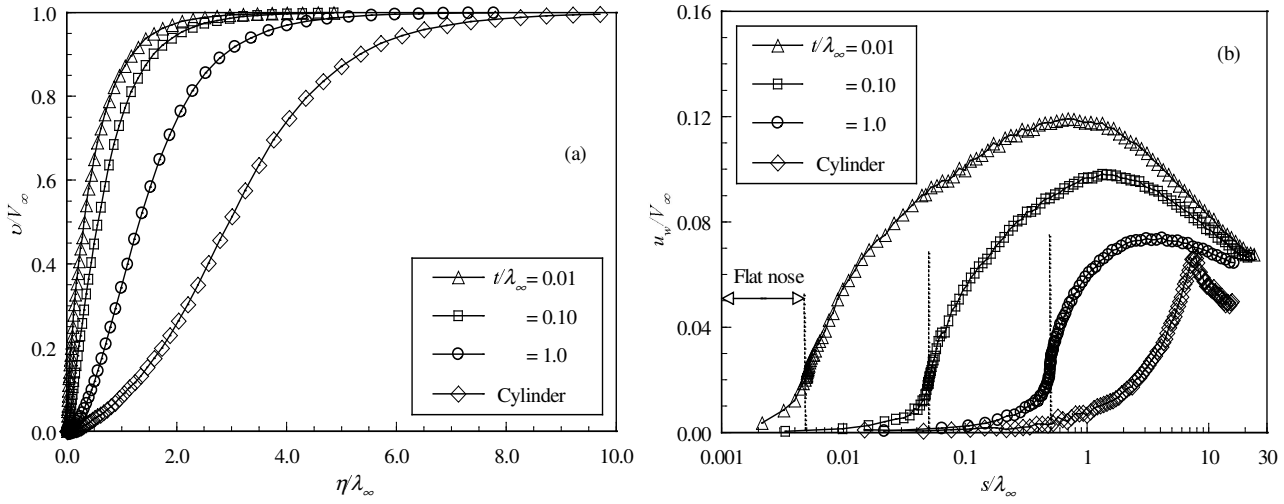

Figure 2: (a) Normal velocity (v/V_∞) profiles along the stagnation streamline, and (b) velocity slip(u_w/V_∞) profiles along the body surface as a function of the leading edge thickness.

Density profiles along the stagnation streamline are plotted as a function of the leading edge thickness in Fig. (3a). The predictions of density for all of the leading edge thicknesses investigated show no sign of a discrete shock wave. Instead, there is a continuous rise in density from the freestream to the nose of the leading edges, rising to well above the continuum inviscid limit. As a point of reference, the Rankine-Hugoniot relations give a postshock density that corresponds to the ratio ρ/ρ_∞ = 5.8 for freestream Mach number of 12. Near the stagnation point (η/λ_∞ = 0), a substantial density increase occurs which is a characteristic of cold-wall entry flow (Haas and Fallavollita, 1994). In typical entry flow, the body surface temperature is low compared to the stagnation temperature. This leads to a steep density gradient near the body surface. For the present simulation, the ratio of wall temperature to stagnation temperature is 0.13, which corresponds to a cold-wall flow.

It can be observed from these density profiles that density rises gradually as the flow approaches the nose of the leading edge, indicating the diffuse nature of the shock wave, a characteristic of highly rarefied flows. As the leading edge becomes blunter, the extent of the flowfield disturbances becomes much larger, as evidenced by the density profiles. For the flow conditions in the present simulation, the free molecular flow equations (Bird, 1994) give a density ratio of 9.89, at the stagnation point for the leading edge shapes. As can be seen, the density ratio for the t/λ_∞ = 0.01 case is approaching the free molecular value at the stagnation point. Unlike normal velocity, density has little effect on the extent of the domain of influence upstream of the body for the leading edge thicknesses investigated. Much of the density increase in the shock layer occurs after the temperature has reached its postshock value, as will be seen later.

Pressure profiles along the stagnation streamline are shown in Fig. (3b) as a function of the leading edge thickness. In this Fig., pressure is normalized by the freestream pressure p_∞. As can be seen, there is a continuous rise in pressure from the freestream up to the nose of the leading edge. Near the stagnation point, a substantial pressure increase occurs with increasing the leading edge thickness t. The extent of the upstream flowfield disturbance for pressure is significantly different from that presented by density. The domain of influence for pressure is higher than that for density and lower than that presented for temperature (shown later). Similar to the density, much of the pressure increase in the shock layer occurs after the translational kinetic temperature has reached its postshock value.

Figures (4a)-(4d) display the kinetic temperature profiles, normalized by the freestream temperature T_∞, along the stagnation streamline for dimensionless leading edge thicknesses of 0.01, 0.1 and 1.0, and for the circular cylinder case, respectively. From these Figs., thermodynamic nonequilibrium is observed throughout the shock layer, as shown by the lack of equilibrium of the translational and internal kinetic temperatures. Thermal nonequilibrium occurs when the temperatures associated with the translational, rotational, and vibrational modes of a polyatomic gas are different.

The overall kinetic temperature shown is defined for a nonequilibrium gas as the weighted mean of the translational and internal temperature (Bird, 1994) as follows,

$$T = \frac{\zeta_T T_T + \zeta_R T_R + \zeta_V T_V}{\zeta_T + \zeta_R + \zeta_V} \tag{2}$$

where ζ is the degree of freedom, and subscripts T, R and V stand for translational, rotational and vibration modes.

It is important to observe that the ideal gas equation of state does not apply to this temperature in a nonequilibrium situation. The overall kinetic temperature is equivalent to the thermodynamic temperature only under thermal equilibrium conditions.

According to Figs. (4a)-(4d), in the undisturbed freestream far from the body, the translational and internal temperatures have the same value and are equal to the thermodynamic temperature. Approaching the nose of the leading edge, the translational temperature rises to well above the rotational and vibrational temperatures and reaches a maximum value that is a function of the leading edge thickness.

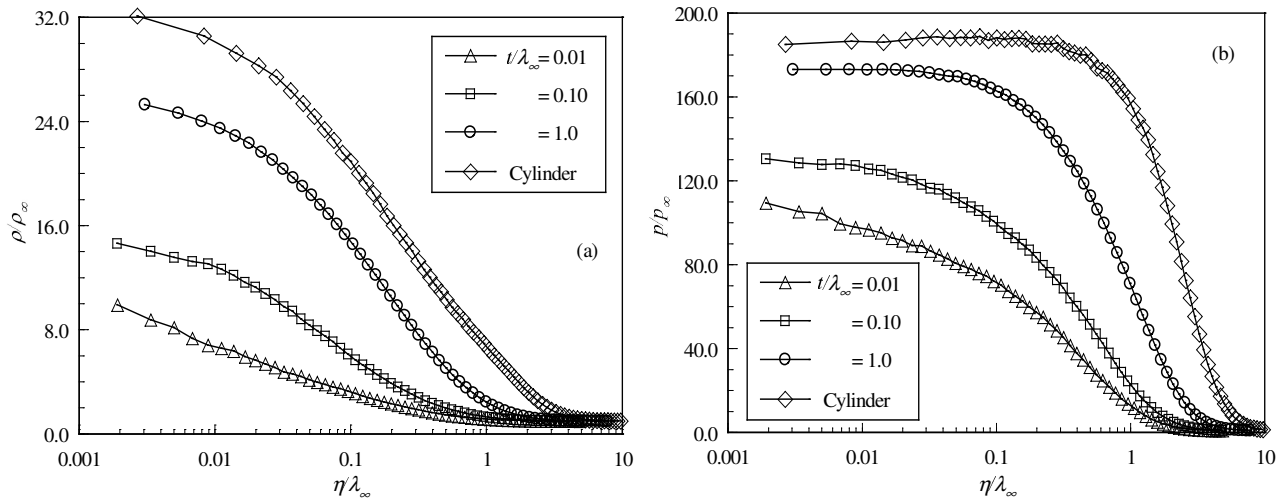

Figure 3: (a) Density (ρ/ρ_∞) and (b) pressure (p/p_∞) profiles along the stagnation streamline as a function of the leading edge thickness.

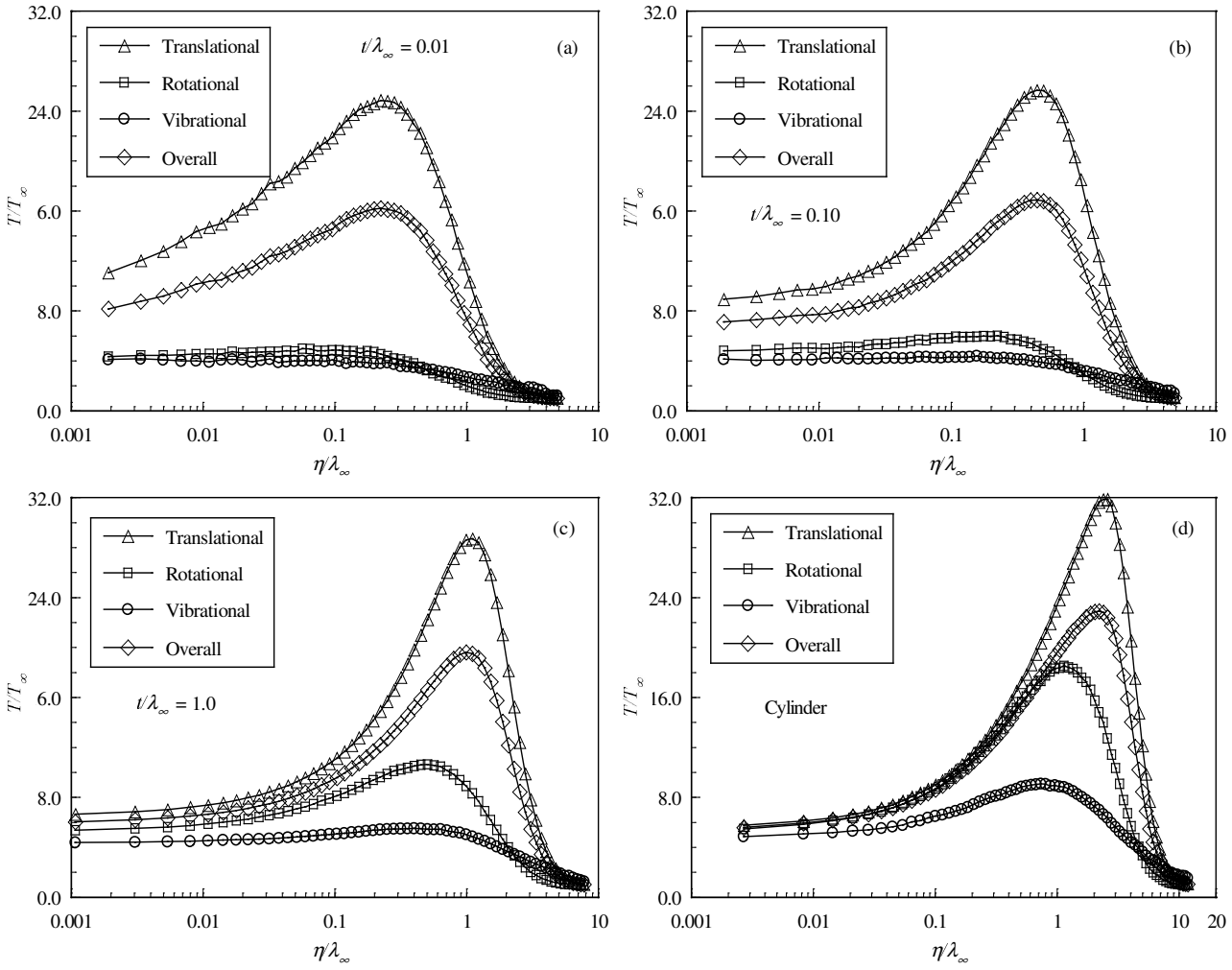

Figure 4: Kinetic temperature (T/T_∞) profiles along the stagnation streamline for leading edge thickness with t/λ_∞ of (a) 0.01, (b) 0.10, and (c) 1.0, and (d) for the circular cylinder case.

Since a large number of collisions is needed to excite molecules vibrationally from the ground state to the upper state, the vibrational temperature increases much more slowly than rotational temperature. Still further downstream toward the nose of the leading edge, the translational temperature decreases and reaches a value on the wall that is above the wall temperature, resulting in a temperature jump as defined in continuum formulation (Gupta et. al., 1985).

The substantial rise in translational kinetic temperature for blunt leading edges occurred before the density rise (see Fig. (3a)). For instance, the kinetic translational temperature reaches the maximum value around a distance of one freestream mean free path from the nose of the leading edge for the t/λ_∞ = 1.0 case, while the density ratio ρ/ρ_∞ is around 2.4 at the same station. The initial translational kinetic temperature rise for blunt leading edges results from the essentially bimodal velocity distribution: the molecular sample consisting of mostly undisturbed freestream molecules with the molecules that have been affected by the shock and reflected from the body. In this way, the translational kinetic temperature rise is a consequence of the large velocity separation between these two classes of molecules. The bimodal velocity distribution was pointed out by Liepmann et al. (1964).

Blunting the leading edge moves the shock wave created during the hypersonic flight forward and out, away from the leading edge, creating an air pocket in front of it. This strong shock wave that forms ahead of a bunt leading edge at hypersonic flow converts the kinetic energy of the freestream air molecules into thermal energy. This thermal energy downstream of the shock wave is partitioned into increasing the translational kinetic energy of the air molecules, and into exciting of other molecular energy states such as rotation and vibration (see Figs. (4a)-(4d)). Most of the energy remains with the air molecules as they flow around the body. As a result, the heat flux to the body surface will be relatively low as compared to sharp leading edges, as shown later.

In an effort to provide additional information concerning the flowfield structure, dimensionless pressure contours and dimensionless overall temperature contours, with streamlines patterns, on color maps, are illustrated in Figs. (5) and (6), respectively, for leading edge thickness t/λ_∞ of 1.0 and for the circular cylinder.

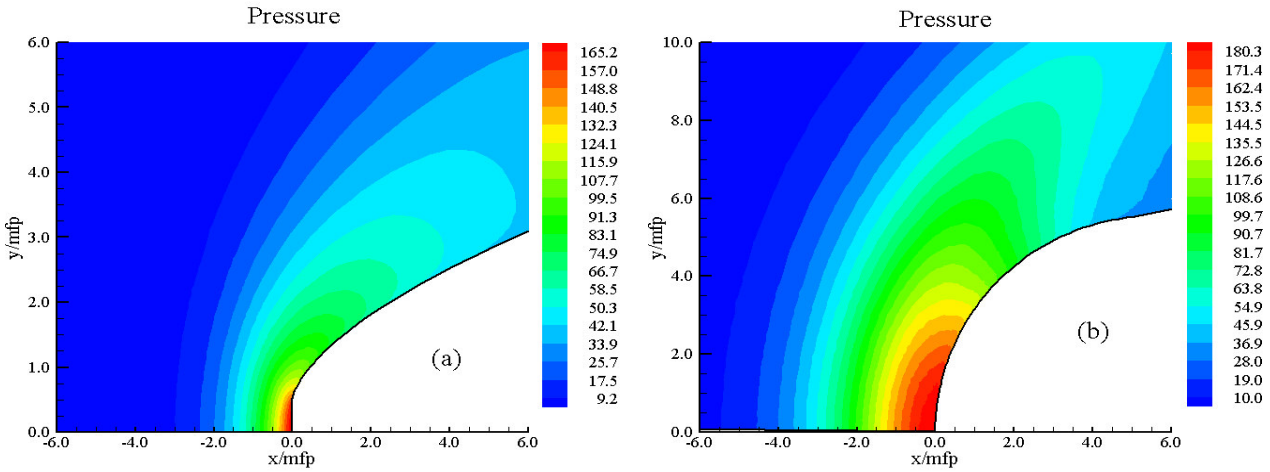

Figure 5: Dimensionless pressure (p/p_∞) contours (a) for t/λ_∞ = 1.0 case and (b) for the circular cylinder case. mfp stands for the freestream mean free path.

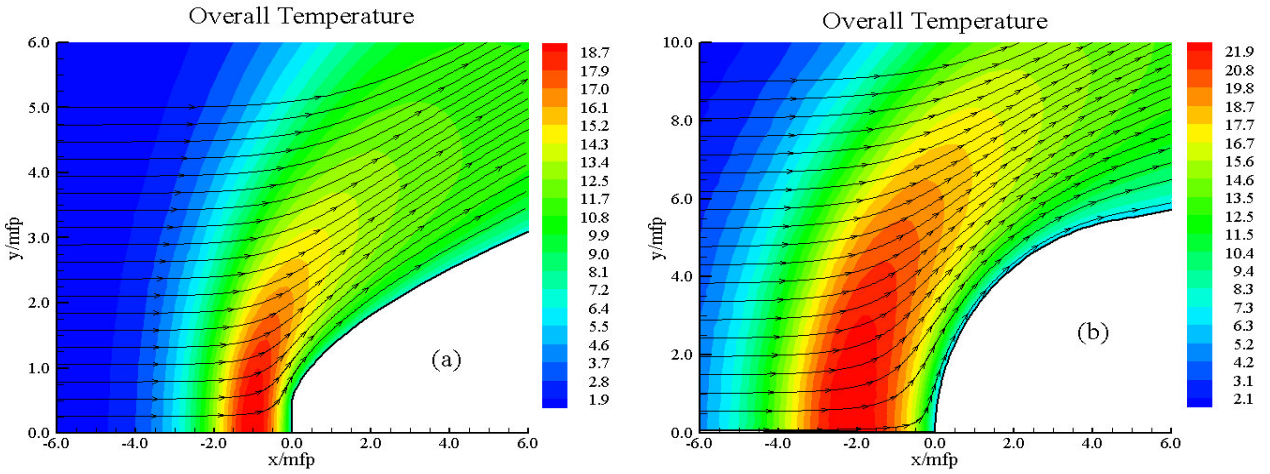

Figure 6: Dimensionless overall temperature (T/T_∞) contours in the vicinity of the leading edge (a) for t/λ_∞ = 1.0 case and (b) for the circular cylinder case. mfp stands for the freestream mean free path.

3.2. Surface Quantities

The number flux N is calculated by sampling the molecules impinging on the surface by unit time and unit area. Results are normalized by $n_\infty V_\infty$, where n_∞ is the freestream number density and V_∞ is the freestream velocity. The sensitivity of the dimensionless number flux to variations on the leading edge thickness is depicted in Fig. (7a) as a function of the dimensionless arc length s/λ_∞, measured from the stagnation point. Also, the dimensionless number flux for the cylinder case and that predicted by assuming free collision flow (Bird, 1994) are included for reference in Fig. (7a).

It is seen from Fig. (7a) that the dimensionless number flux is high near the stagnation point and slightly decreases along the front surface up to the flat nose/afterbody junction. After that, it drops off sharply along the body surface. The qualitative trend for the dimensionless number flux is as expected, approaching the limit value obtained by the free molecular flow equations as the leading edge thickness decreases, i.e., as the leading edge becomes sharp.

According to Fig. (7a), the dimensionless number flux to the front surface relies on the leading edge thickness in that it increases with the thickness t. One possible reason for this behavior may be related to the collisions of two groups of molecules; the molecules reflecting from the nose of the leading edge and the molecules oncoming from the freestream. The molecules that are reflected from the body surface, which have a lower kinetic energy interact with the oncoming freestream molecules, which have a higher kinetic energy. Thus, the surface-reflected molecules recollide with the body surface, which produce an increase in the dimensionless number flux in this region.

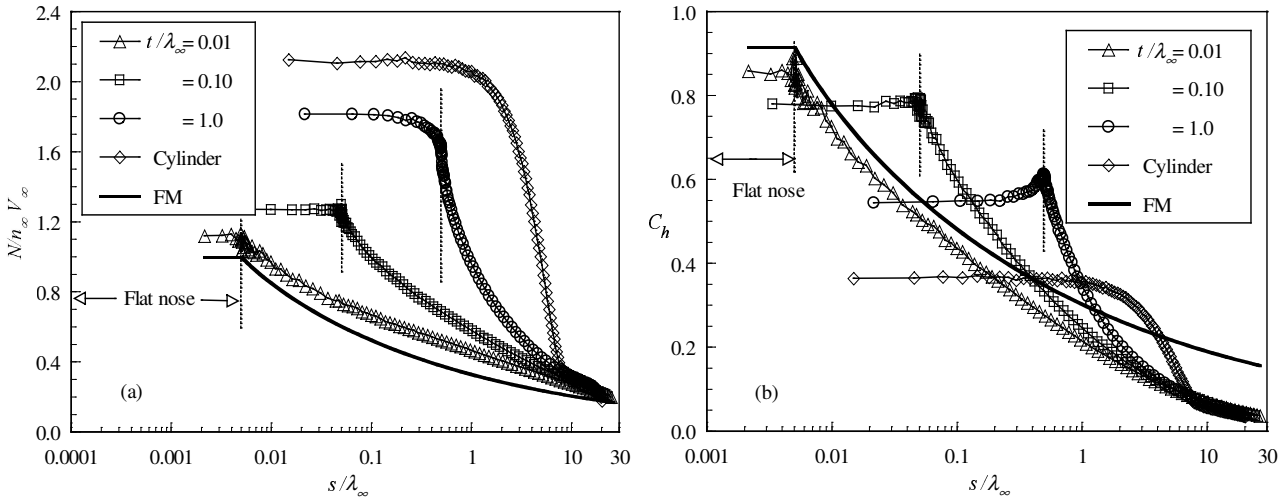

Figure 7: (a) Dimensionless number flux ($N/n_\infty V_\infty$) and (b) heat transfer coefficient along the body surface as a function of the leading edge thickness.

The heat flux q_w to the body surface is calculated by the net energy fluxes of the molecules impinging on the surface. The net heat flux is related to the sum of the translational, rotational and vibrational energies of both incident and reflected molecules. A flux is regarded as positive if it is directed toward the surface. The heat flux is normalized by $\frac{1}{2}\rho_\infty V_\infty^3$ and presented in terms of heat transfer coefficient C_h.

The heat flux was based upon the gas-surface interaction model of fully accommodated, completely diffuse re-emission. This is the most common model assumed, even though it is well known that some degree of specular re-emission and less than complete accommodation are more realistic assumptions. Furthermore, care should be taken in choosing the thermal accommodation coefficient for different altitude ranges, since the value of a thermal accommodation coefficient has a significant impact on the prediction of the aerodynamic heating, as pointed out by Gilmore and Harvey (1994).

The leading edge thickness effect on heat transfer coefficient is plotted in Fig. (7b) as a function of the dimensionless distance s/λ_∞ along the surface measured from the stagnation point. For comparison purpose, the heat transfer coefficient predicted by free molecular flow is also shown as well as that for the circular cylinder case. It is seen from Fig. (7b) that the heat transfer coefficient is sensitive to the leading edge thickness. As would be expected, the blunter the leading edge is the lower the heat transfer coefficient at the stagnation point. Also, the heat transfer coefficient remains essentially constant over the first half of the front surface, but then increases in the vicinity of the flat nose/afterbody junction for the bluntest case investigated, t/λ_∞ = 1.0. Subsequently, the heat transfer coefficient decreases sharply and continues to decline along the body surface. In contrast, for the circular cylinder, the heat transfer coefficient remains essentially constant over the first half of the cylindrically portion of the leading edge, but then decreases sharply up to the cylinder/wedge junction. With respect to the stagnation point, the heat transfer coefficient for shapes t/λ_∞ = 0.01, 0.1 and 1.0 corresponds, respectively, to 2.4, 2.2 and 1.5 times the heat transfer coefficient for the circular cylinder.

The heat flux to the body surface was defined in terms of the incident and reflected flow properties. In order to

better visualize the behavior of the heat transfer coefficient on the body surface, the incident C_{hi} and reflected C_{hr} contributions to the heat transfer coefficient C_h are illustrated in Figs. (8a) and (8b), respectively. According to these Figs., it is observed that the incident and reflected contributions present different behaviors. The difference is associated to the gas-surface interaction. The diffuse model assumes that molecules are reflected equally in all directions, quite independently of their incident speed and direction. Due to the diffuse reflection model, the reflected thermal velocity of the molecules impinging on the surface is obtained from a Maxwellian distribution that takes into account for the temperature of the body surface. In this fashion, as the wall temperature is the same for all the cases investigated, the number of molecules impinging on the surface plays the important role on the reflected contribution to the net heat flux to the body surface.

The heat transfer coefficient behavior is as expected since the thermal velocity of the molecules increases near the flat nose/afterbody junction. Moreover, the contribution of the translational energy to the net heat flux varies with the square of the thermal velocity of the molecules.

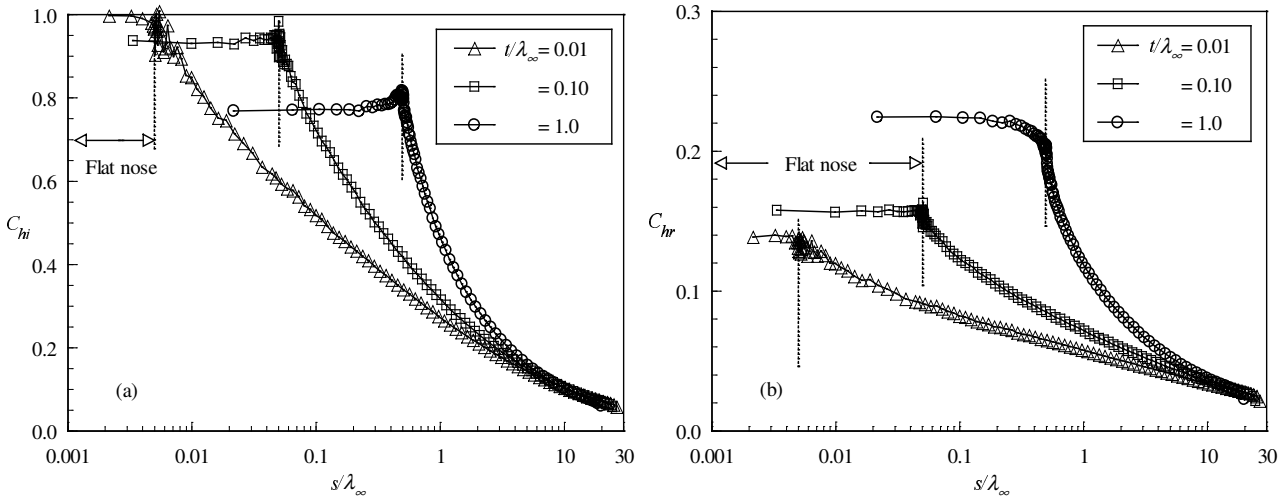

Figure 8: (a) Incident heat transfer coefficient and (b) reflected heat transfer coefficient along the body surface as a function of the leading edge thickness.

The pressure p_w on the body surface is calculated by the sum of the normal momentum fluxes of both incident and reflected molecules at each time step. Results are normalized by the freestream dynamic pressure $\frac{1}{2}\rho_\infty V_\infty^2$ and presented in terms of the pressure coefficient C_p.

The effects of the leading edge thickness on the pressure coefficient are demonstrated in Fig. (9a). Plotted along with the computational solution for pressure coefficient is the pressure coefficient predicted by the free molecular flow equations and that for the circular cylinder. Referring to Fig. (9a), it can be seen that the pressure coefficient is basically constant along the front surface, and this constant value increases with increasing Knudsen number Kn_t. For the circular cylinder case, the pressure coefficient follows the same trend presented by the heat transfer coefficient in that it remains constant over the first half of the cylindrically portion of the leading edge, but then decreases sharply up to the cylinder/wedge junction.

The pressure coefficient predicted by the free molecular flow equations on the front surface is 2.35. Therefore, for the thinnest blunt leading edge (t/λ_∞ = 0.01) investigated, the flow seems to approach the free collision flow in the vicinity of the stagnation point (Fig. (9a)), as was pointed out earlier.

The shear stress τ_w on the body surface is calculated by averaging the tangential momentum transfer of the molecules impinging on the surface. For the diffuse reflection model imposed for the gas-surface interaction, reflected molecules have a tangential moment equal to zero, since the molecules essentially lose, on average, their tangential velocity component.

The shear stress τ_w on the body surface is normalized by $\frac{1}{2}\rho_\infty V_\infty^2$ and presented in terms of the dimensionless skin friction coefficient C_f. The influence of the leading edge thickness on the skin friction coefficient obtained by DSMC method is displayed in Fig. (9b), parameterized by the dimensionless leading edge thickness.

According to Fig. (9b), the skin friction coefficient is zero at the stagnation point and slightly increases along the front surface up to the flat nose/afterbody junction of the leading edge. After that, it increases dramatically to a maximum value that depends on the leading edge thickness, and decreases downstream along the body surface. Smaller thickness t leads to higher peak value for the skin friction coefficient. Also, smaller thickness t displaces the peak value to near the front surface/afterbody junction.

The skin friction coefficient predicted by the free molecular flow exhibits its maximum value at a station that corresponds to a body slope of 45°. Similarly, the maximum values for the leading edge thicknesses investigated occur very close to the same station. The number of molecules by unit time and unit area impinging on the body is high on the front surface of the leading edge and low on the afterbody portion of the body (see Fig. (7a)). In contrast, the

tangential component of the thermal velocity is basically zero on the front surface and high along the afterbody surface (due to the flow expansion), where the velocities of the molecules are those that are more characteristic of the freestream velocity. As a result, the product of both properties, which is proportional to the skin friction coefficient, presents the maximum value around station of 45°. Furthermore, attention should be paid to the fact that a body slope of 45° corresponds to different arc length s/λ_∞ for the leading edge thicknesses investigated, since the exponent k, that appears in Eq.(1), is different for each case.

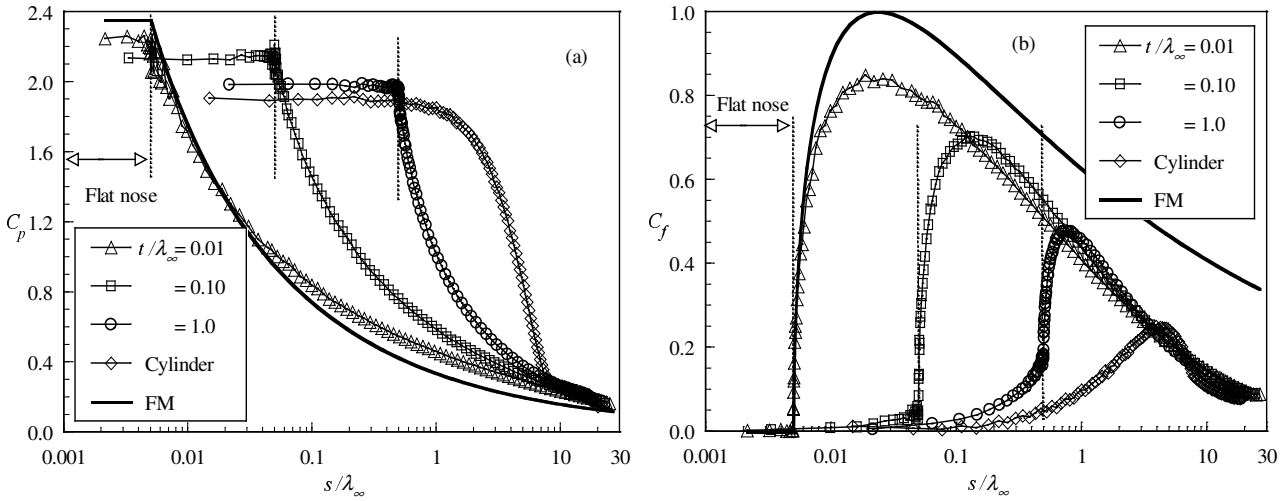

Figure 9: (a) Pressure coefficient and skin friction coefficient along the body surface as a function of the leading edge thickness.

The drag on a surface in a gas flow results from the interchange of momentum between the surface and the molecules colliding with the surface. The total drag is obtained by the integration of the pressure p_w and shear stress τ_w distributions from the stagnation point of the leading edge to the station L that corresponds to the tangent point common to all the leading edges (see Fig. (1a)). It is worthwhile to mention that the values for the total drag were obtained by assuming the shapes acting as leading edges. Therefore, no base pressure effects were taken into account on the calculations. The DSMC results for total drag are normalized by $\frac{1}{2}\rho_\infty V_\infty^2 H$ and presented as total drag coefficient C_d and its components of pressure drag coefficient and the skin friction drag coefficient.

The extent of the changes in the drag coefficient C_d with increasing the leading edge thickness is demonstrated in Fig. (10a) along with the drag coefficient for the circular cylinder. It is seen that as the leading edge becomes blunt the contribution of the pressure drag to the total drag increases and the contribution of the skin friction drag decreases. As the net effect on total drag coefficient depends on these to opposite behaviors, hence appreciable changes are observed in the total drag coefficient for the leading edge thicknesses investigated. As a reference, the drag coefficient for the $t/\lambda_\infty = 1.0$ case is around 8% higher than that for the $t/\lambda_\infty = 0.01$ case.

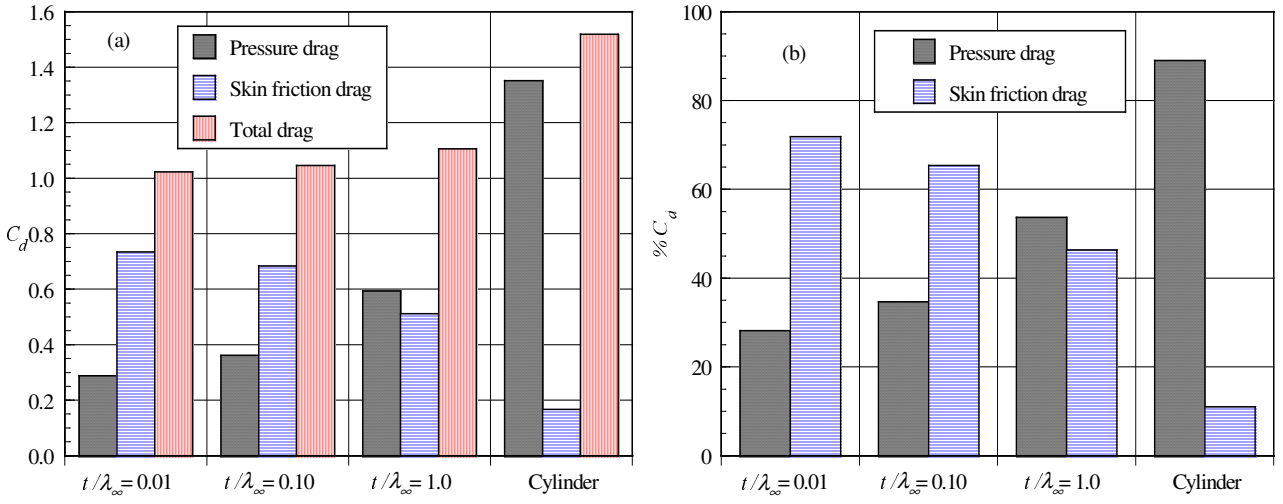

Figure 10: (a) Pressure drag, skin friction drag and total drag coefficients for blunt shapes and circular cylinder, and (b) percentage of pressure drag and skin friction drag coefficients to the total drag coefficient.

For the circular cylinder, the pressure drag, skin friction drag and the total drag are 1.352, 0.167 and 1.519, respectively. In this way, the total drag for the circular cylinder is 48.5%, 45.3% and 37.4% higher than the total drag for shapes t/λ_∞ = 0.01, 0.1 and 1.0, respectively. Thus, compared to the blunt shapes, the circular cylinder presents a high value for the total drag coefficient, where the major contribution is given by the pressure coefficient.

The fraction of pressure drag to total drag as well as the fraction of skin friction drag to total drag is depicted in Fig. (10b) for the cases investigated. As shown, for the t/λ_∞ = 0.01 case, the shear forces account for more than 70% of the total drag on the leading edge, whereas for the t/λ_∞ = 1.0 case, it accounts for less than 50%. In contrast, for the circular cylinder, the skin friction drag contribution is only of 10%.

4. Concluding Remarks

The computations of a rarefied hypersonic flow on blunt leading edges have been performed by using the Direct Simulation Monte Carlo method. The calculations provided information concerning the nature of the flow structure and the aerodynamic surface quantities at the vicinity of the nose for a family of contours composed by a flat nose followed by a highly curved aferbody surface.

The aerodynamic performance of these blunt shapes was compared to a corresponding circular cylinder leading edge shape, typically used in blunting sharp leading edges for heat transfer considerations. It was found that the stagnation point heating is higher and the total drag is lower on the new blunt shapes than the representative circular cylinder solution in this geometric comparison. Thus, in general, these shapes behave as if they had a sharper profile than their representative circular cylinder. However, these shapes have more volume than the circular cylinder geometry. Hence, although stagnation point heating on these new shapes may be higher, the overall heat transfer to these leading edges may be tolerate if there is active cooling because additional coolant may be placed in the leading edge. Moreover, shock standoff distance on a cylinder scales with the radius of curvature, therefore cylindrical bluntness added for heating rate reduction will also tend to displace the shock wave, allowing pressure leakage. In this context, as the new shapes behave as if they were sharper profiles than the circular cylinder, they may display smaller shock detachment distances than the corresponding circular cylinder. Nevertheless, the shock wave structure on these new shapes is the subject for future work.

5. References

Bertin, J. J., 1994, "Hypersonic Aerothermodynamics", AIAA Education Series, Washington D.C..

Bird, G. A., 1981, "Monte Carlo Simulation in an Engineering Context", Progress in Astronautics and Aeronautics: Rarefied gas Dynamics, Ed. Sam S. Fisher, Vol. 74, part I, AIAA New York, pp. 239-255.

Bird, G. A., 1994, "Molecular Gas Dynamics and the Direct Simulation of Gas Flows", Oxford University Press, Oxford, England, UK.

Borgnakke, C. and Larsen, P. S., 1975, "Statistical Collision Model for Monte Carlo Simulation of Polyatomic Gas Mixture", Journal of computational Physics, Vol. 18, pp. 405-420.

Eggers, A. J., Jr., Resnikoff, Meyer, M. and Dennis, D. H., 1956, "Bodies of Revolution Having Minimum Drag at High Supersonic Airspeeds", NACA TN-3666.

Gilmore, M. R. and Harvey, J. H., 1994, "Effects of Mach Number, T_{wall}, T_∞ and Thermal Accommodation Coefficient on Flow Around Bluff Bodies in Rarefied Regime", Rarefied Gas Dynamics: Space Science and Engineering, edited by B. D. Shizgal and D. P. Weaver, Vol. 160, Progress in Astronautics and Aeronautics, AIAA New York, pp. 308-322.

Gupta, R. N., Scott, C. D., and Moss, J. N., 1985, "Slip-Boundary Equations for Multicomponent Nonequilibrium Airflow", NASA TP-2452.

Haas, B. L., Fallavollita, M. A., 1994, "Flow Resolution and Domain Influence in Rarefied Hypersonic Blunt-Body Flows", Journal of Thermophysics and Heat Transfer, Vol. 8(4), pp. 751-757.

Liepmann, H. W., Narasimha, R. and Chahine, M., 1964, "Theoretical and Experimental Aspects of the Shock Structure Problem", Proceedings of the 11th International Congress of Applied Mechanics, Ed. H. Gortler, Munich, Germany, pp. 973-979.

Reller Jr., J. O., 1957, "Heat Transfer to Blunt Nose Shapes with Laminar Boundary Layers at High Supersonic Speeds", NACA RM-A57FO3a.

Schaff, S. and Chambre P., 1958, “Fundamentals of Gas Dynamics”, Princeton University Press, Princeton, NJ.